

Review

Restriction of molecular motion to a higher level: Towards bright AIE dots for biomedical applications

Changhuo Xu,^{1,5} Hanchen Shen,^{1,5} Tzu-Ming Liu,³ Ryan T.K. Kwok,¹ Jacky W.Y. Lam,^{1,*} and Ben Zhong Tang^{2,4,*}

SUMMARY

In the late 19th century, scientists began to study the photophysical differences between chromophores in the solution and aggregate states, which breed the recognition of the prototypical processes of aggregation-caused quenching and aggregation-induced emission (AIE). In particular, the conceptual discovery of the AIE phenomenon has spawned the innovation of luminogenic materials with high emission in the aggregate state based on their unique working principle termed the restriction of intramolecular motion. As AIE luminogens have been practically fabricated into AIE dots for bioimaging, further improvement of their brightness is needed although this is technically challenging. In this review, we surveyed the recent advances in strategic molecular engineering of highly emissive AIE dots, including nanoscale crystallization and matrix-assisted rigidification. We hope that this timely summary can deepen the understanding about the root cause of the high emission of AIE dots and provide inspiration to the rational design of functional aggregates.

INTRODUCTION

The history of molecular fluorescence dates back to the mid-16th century. Nicolás Monardes, a Spanish physician and botanist, was the first to describe the blue opalescence of liquid extract when *Lignum nephriticum* cups were filled with water. Such a fluorescence phenomenon was coined “internal dispersion” by David Brewster in 1838 when he observed the fluorescence of chlorophyll from an alcohol solution of leaves.¹ Seven years later, John Herschel, an English polymath, reported the celestial blue fluorescence of quinine sulfate in tartaric acid solution in his publication, whose chemical structure is shown in Figure 1A.³ Although most researchers in that period declared their discoveries of fluorescent substances in the solution state, few of them had paid attention to the optical properties of their solids and their differences with those in the solution state until George Stokes published his 100-page monograph in 1852 describing a vast collection of fluorescent substances, including quinine sulfate.⁴ He documented that crystals of quinine sulfate are “much less sensitive than their solution”, representing an inchoate prototype of the concentration-quenching (CQ) effect. A similar observation was recorded in Henry Morton’s publication in 1871, stating that dilution of a saturated acid solution of quinine sulfate can enhance its fluorescence.⁵ As depicted in Figure 1A, on aggregate formation in water/tetrahydrofuran (THF) mixtures with high THF volume fractions, the decreased fluorescence of quinine sulfate distinctly validates the phenomenon known as aggregation-caused quenching (ACQ). Besides, the CQ or ACQ process was widely identified in other organic dyes, such as chlorophyll, uranine, and pyrene.^{6,7}

While exploring the molecular fluorescence in solution, scientists were acutely aware of the strong fluorescence from inorganic salts. In George Stokes’ treatise, he mentioned the first observation of green fluorescence from barium platinocyanide powders. On the contrary, he described the fluorescence of its solution as “mere water”.⁴ In 1871, Henry Morton also reported the “brilliant green fluorescence” of uranium nitrate solids and additionally said that its emission in solution was feeble, even though the “fluorescence” of nitrate of uranium was later found to be phosphorescence in nature.^{8–10} Since then, a growing number of scholars noted the emission of some organic dyes in the solid state excelling that of the corresponding solution ones, whereas the structure-property relationship and underlying mechanism remained obscure for decades in the academic community.^{11,12} In 2001, a serendipitous luminescence study of silole conducted by Tang et al. unveiled the prelude of the journey of aggregation-induced emission (AIE).^{13,14} The AIE

¹Department of Chemistry, Hong Kong Branch of Chinese National Engineering Research Center for Tissue Restoration and Reconstruction, Division of Life Science, State Key Laboratory of Molecular Neuroscience, Guangdong-Hong Kong-Macau Joint Laboratory of Optoelectronic and Magnetic Functional Materials, The Hong Kong University of Science and Technology, Clear Water Bay, Kowloon, Hong Kong, China

²School of Science and Engineering, Shenzhen Key Laboratory of Functional Aggregate, The Chinese University of Hong Kong, Shenzhen, Guangdong 518172, China

³Institute of Translational Medicine, Faculty of Health Sciences, University of Macau, Macao, China

⁴Center for Aggregation-Induced Emission, South China University of Technology, Guangzhou 510640, China

⁵These authors contributed equally

*Correspondence: chjacky@ust.hk (J.W.Y.L.), tangbenz@cuhk.edu.cn (B.Z.T.)

<https://doi.org/10.1016/j.isci.2023.106568>



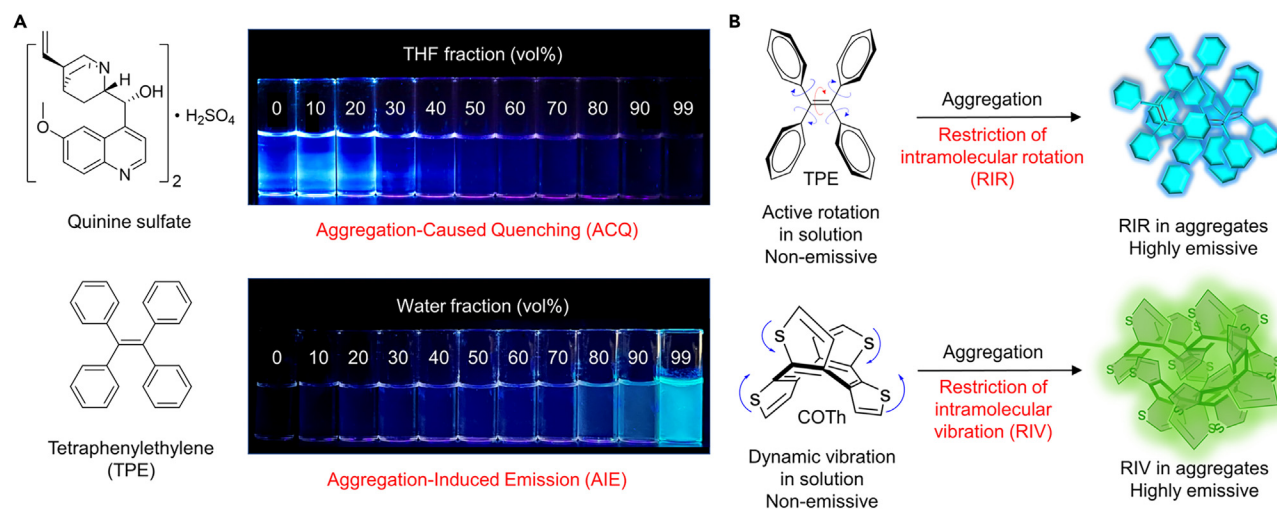


Figure 1. Processes of aggregation-caused quenching (ACQ) and aggregation-induced emission (AIE)

(A) Chemical structures of representative fluorogens with ACQ or AIE characteristics: quinine sulfate and tetraphenylethylene (TPE), and their fluorescent photographs in tetrahydrofuran (THF)/water mixtures with different THF or water fractions taken under 365 nm UV light irradiation. (B) Typical examples of AIE luminogens: TPE and cyclooctatetrathiophene (COTh), whose AIE processes are mainly caused by the restriction of intramolecular rotation (RIR) and vibration (RIV), respectively. Reproduced with permission from Wiley.² Copyright 2022 Wiley-VCH.

phenomenon can be exemplified by an iconic AIE luminogen (AIEgen) named tetraphenylethylene (TPE), as illustrated in Figure 1A.¹⁵ In THF, it exhibits no emission as a molecular species. Once a large volume of water as an antisolvent is added to trigger the aggregation of TPE molecules, the emission increases dramatically. Thus, AIE is an inverse process of the ACQ effect. Based on the comprehensive investigation of available AIEgens, in an either experimental or theoretical way, the physical picture of AIE phenomenon has been gradually deblurred toward extensive recognition by academia. It is proved that the active excited-state intramolecular motion of AIEgens, comprising intramolecular rotation and vibration, can facilitate the nonradiative decay and quench their fluorescence in solution (Figure 1B).^{2,16} On aggregation, the formed mutual interactions restrict the intramolecular motion to block the nonradiative decay pathway to lead to emission enhancement. The clarified mechanism of AIE is eventually generalized to restriction of intramolecular motion (RIM), including restriction of intramolecular rotation (RIR) and restriction of intramolecular vibration (RIV).

Given the bright emission of AIEgens in the aggregate state, together with their large Stokes shift, free of random blinking, and photobleaching resistance, they are perfect candidates for hierarchical bioimaging from cell models to living animals once formulated into AIE dots.^{17,18} To improve the brightness of AIE dots, nanoscale engineering of AIEgens using physical approaches is much preferred because of their universal applicability for all the AIEgens.¹⁹ In terms of the RIM mechanism, the AIE effect can be strengthened by regulating environmental factors far out of normal values, such as low temperature, high viscosity, high pressure, etc., whereas these approaches are inaccessible for practical bioimaging operations.^{20–22} In most cases, AIEgens need to be encapsulated into biocompatible matrices to afford stable dispersion in an aqueous medium for long-term imaging.²³ Therefore, direct manipulation of homotypic interactions between AIEgens or heterotypic interactions between matrices and AIEgens is a more feasible way to achieve the high brightness of AIE dots. In this review, we summarize the recent advances in the fabrication of highly emissive AIE dots through nanoscale crystallization and matrix-assisted rigidification. Common nanocrystallization methods can be classified as natural aging, sonication-augmented crystallization and nanoconfined crystallization. Based on previously reported literature, biocompatible matrices adopted for structural rigidification of AIEgens mainly consist of proteins, rigid polymeric matrices, and silicon dioxide. Typical examples will be elaborated as follows.

NANOSCALE CRYSTALLIZATION

Theoretically, ordered arrangement in crystals can provide one of the most rigid environments for the accommodation of AIEgens. Such an empirical inference can be distinctly embodied in a portion of AIE systems. For example, amorphous powders of BpPDBF and CMVMN emit dim emission with a negligible

photoluminescence quantum yield (PLQY) of 0.5%. In comparison, their quantum yields in the crystalline state can reach 16% and 63%, respectively (Figure 1A).^{24,25} A near-infrared (NIR)-II AIEgen named TPE-BBT shows an impressive absolute PLQY of 2.1% in the aggregate state. Upon crystallization, its PLQY is boosted to 10.4%, which is the highest absolute PLQY ever reported in the NIR-II region.²⁶ These results demonstrate that the strong intermolecular interactions in crystals can largely restrain the molecular motion of AIEgens so that the radiative decay is dominated for the emission enhancement. In contrast, the mutual rigidification effect within AIEgens in the amorphous state is impaired to result in a weak emission. In practice, the rapid fabrication process of AIE dots under kinetic control often leads to irregular packing of AIEgens with low crystallinity and low fluorescence efficiency. Therefore, as an efficient way to improve the brightness of AIE dots, nanocrystallization is very promising but technically challenging.

Natural aging

By natural aging, the amorphous aggregates formed by AIEgens in organic/water mixtures can spontaneously evolve into a more stable assembly with the help of energy input from environmental perturbations. However, the preparation of nanocrystals (NCs) through the natural aging of nanoaggregates requires unique properties of AIEgen, otherwise these nanoaggregates inevitably form micron-sized precipitates.²⁷ Zheng et al. reported a NIR emissive AIEgen called DCCN with a donor- π -acceptor structure (Figure 2B).²⁸ They prepared a DCCN nanosuspension in an acetone/water mixture with a water volume fraction of 50% (f_w). In the time course of standing at room temperature, its emission gradually increased and showed a 4.5-fold increase in 2 h. Scanning electron microscopic (SEM) images in Figure 2C display that the nanoaggregates experienced a transformation process with polymorphous structures, including spherical aggregates, fibers, and microblocks. By adjusting f_w to 60, 70, or 80%, the nanosuspension of DCCN showed a similar evolution behavior. The size of the obtained blocks decreased on increasing f_w , as depicted in Figure 2D. Especially, the size of the crystals formed at $f_w = 80\%$ was measured to be 129 nm. The crystalline nature of these NCs was further verified by X-ray diffraction (XRD). To ensure water-dispersibility and biocompatibility for *in vivo* bioimaging, the NCs were dispersed in an aqueous solution using Pluronic F127 to afford crystalline dots (CDs). Accordingly, amorphous dots (ADs) were prepared as a comparison and were less emissive than CDs (Figure 2B). Besides, Xu et al. synthesized donor-acceptor-structured AIEgens called DTPA-BT-F and DTPA-BT-H for super-resolution imaging (Figure 2E).²⁹ In a THF/water mixture with $f_w = 60\%$, they observed that the emission of DTPA-BT-F and DTPA-BT-H suspensions showed a time-dependent enhancement. Notably, the emission enhancement of DTPA-BT-F was accompanied with a blue-shift in emission wavelength, implying a significant morphological change (Figure 2F). Analyses by transmission electron microscopy (TEM) and selected area electron diffraction (SAED) were performed to monitor the aggregate evolution. In the beginning, DTPA-BT-F molecules were clustered into amorphous micron-sized aggregates, followed by conversion into nanoparticles (NPs). Highly emissive NCs were finally formed after 6 days' incubation as proved by the SAED pattern. Referring to the explanation of the crystallization-induced emission phenomenon, the red-shifted emission of the amorphous aggregates is because their loose packing enables free molecular motion to give access to an excited-state minimum with a small band gap.¹⁴ In the crystalline state, conformational rigidification blocks the access to lead to enhanced emission with a blue-shift in emission wavelength. Given that natural aging was a time-consuming process with the undesired production of large precipitates, they introduced a nanoprecipitation method using DSPE-PEG as a surfactant for rapid crystal preparation (Figure 2G). As displayed in Figure 2H, nanoprecipitation of DTPA-BT-H only generated amorphous NPs after 2 h. As opposed to DTPA-BT-H, DTPA-BT-F could form NCs after nanoprecipitation relying on the much strengthened intermolecular interactions by fluorine atoms. The monodispersed property and excellent colloidal stability of DTPA-BT-F NCs further laid a solid foundation for their cell imaging study. Based on this work, they also adopted the same method to prepare AIE NCs of DTPA-BS-F for efficient reactive oxygen species (ROS) generation in cancer therapy.³⁰ Overall, the use of natural aging for nanocrystal preparation greatly leans on the unique features of the molecules *per se*, which is not generalizable to all AIEgens.

Sonication-augmented crystallization

The evolution of amorphous nanoaggregates into NCs is a dynamic process involving the dissolution of aggregates and precipitation of dissolved molecules to remodel the spatial packing, where proper energy supply is highly demanded if the energy barrier is too high to get over. Because of this, one of the commonly used processing methods is ultrasonication. For example, Koenig et al. demonstrated an AIE-active fluorescent molecular rotor namely 4-(diphenylamino)-phthalonitrile (DPAP) and studied the morphological change of DPAP aggregates when applying ultrasonication (Figure 3A).³¹ Sonochemical

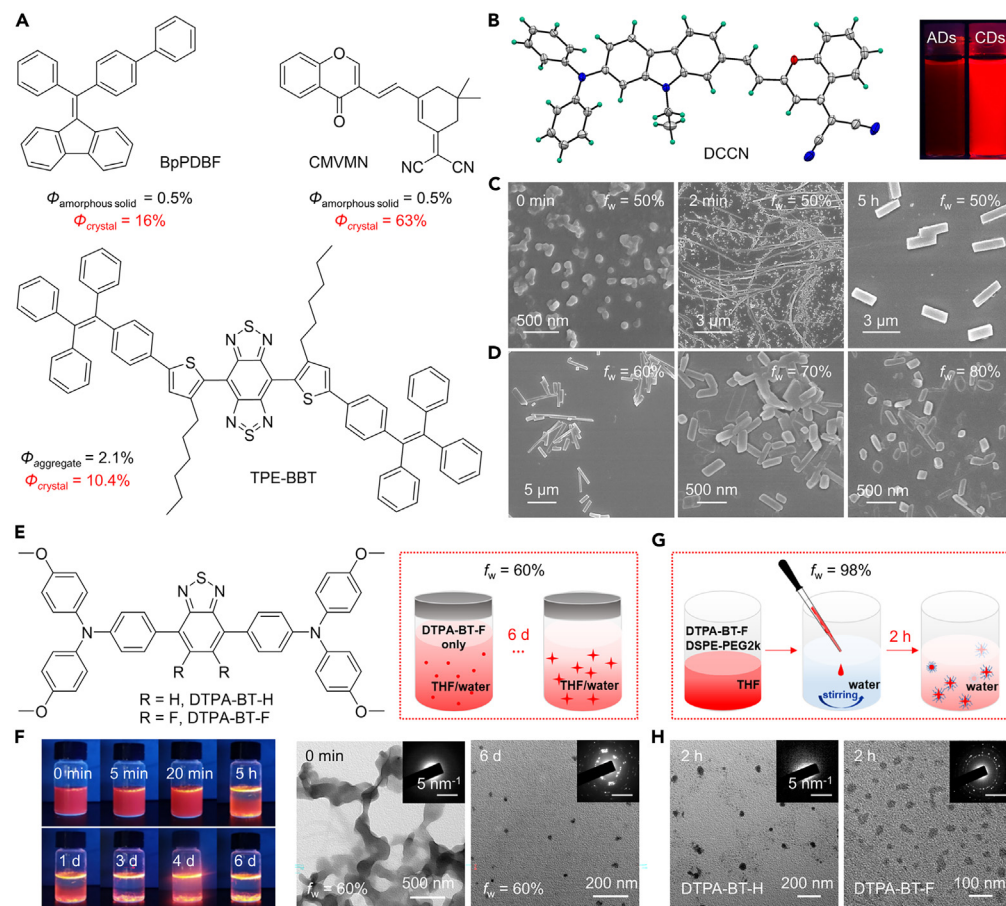


Figure 2. Nanocrystallization via natural aging

(A) Chemical structures of representative AIEgens showing crystallization-induced or crystallization-enhanced emission characteristics.

(B) Single-crystal structure of DCCN and fluorescent photographs of F127-wrapped amorphous dots (ADs) and crystalline dots (CDs) of DCCN in water taken under daylight and UV light irradiation.

(C) SEM images of DCCN in an acetone/water mixture with a water volume fraction (f_w) of 50% taken at different storage times.

(D) SEM images of DCCN nanoparticles after evolving in acetone/water mixtures with f_w at 60%, 70%, 80%, respectively. Reproduced with permission from Wiley.²⁸ Copyright 2019 WILEY-VCH.

(E) Chemical structures of DTPA-BT-H and DTPA-BT-F and schematic illustration of the preparation of nanocrystals through natural aging in a slow way.

(F) Fluorescent images of the evolving DTPA-BT-F nanoaggregates in a THF/water mixture with f_w at 60% and the corresponding TEM images and their corresponding SAED patterns at 0 min and 6 d.

(G) Schematic illustration of the preparation of nanocrystals by the nanoprecipitation method in a fast way.

(H) TEM images of DTPA-BT-H NPs and DTPA-BT-F NCs prepared by the nanoprecipitation method. Insets are their corresponding SAED patterns. Reproduced with permission from RSC.²⁹ Copyright 2022 the Royal Society of Chemistry.

treatment of a dilute DPAP solution ($c = 4.5 \times 10^{-5}$ M) in the water/methanol mixture (87/13, v/v) for 1 min caused an emission increase by 3-fold with a blue-shift in emission maximum from 500 to 470 nm. The ultrasonicated dispersion of DPAP with a high concentration ($c = 2.5 \times 10^{-4}$ M) showed the presence of flat rhomboidal crystals with an average thickness of 30–35 nm and the symmetric SAED pattern supported their crystalline nature (Figure 3B). Li et al. reported the synthesis of three flavonol NCs with AIE characteristics.³² Taking myricetin as an example, by adding its ethanol solution to water that was pre-chilled at 4 °C to decrease its solubility, the rapid nanoprecipitation enabled the preparation of myricetin NCs, during which an ultrasonic probe was used to facilitate the nanocrystallization. The SEM image shown in Figure 3C suggests the formation of monodispersed rod-shaped NCs with an average size of 385 nm. When myricetin was dissolved in ethanol, it emitted negligible fluorescence. On nanocrystallization, strong enol emission

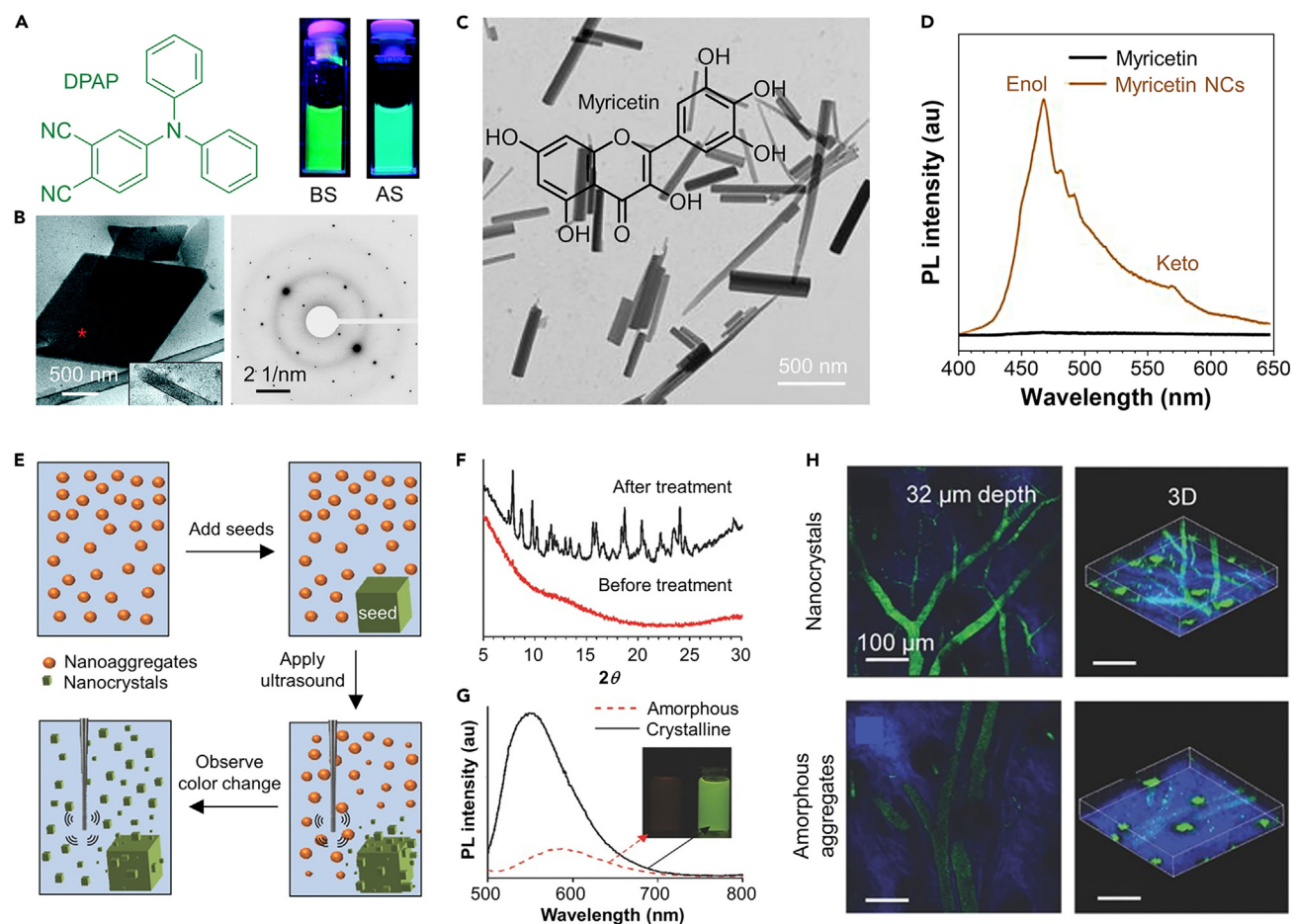


Figure 3. Sonication-augmented crystallization

(A) Chemical structure of DPAP and fluorescent photographs of its nanosuspensions in 87/13 (v/v) water/methanol mixtures before and after sonication treatment (named as BS and AS, respectively). DPAP concentration: 4.5×10^{-4} M.
(B) Cryo-TEM image of a dispersion of DPAP in the water/methanol mixture (87/13, v/v) after sonication and the SAED pattern in the red spot region. DPAP concentration: 2.5×10^{-4} M. Reproduced with permission from RSC.³¹ Copyright 2014 the Royal Society of Chemistry.
(C) Chemical structure of myricetin and SEM image of its NCs prepared through a sonication method.
(D) Photoluminescence (PL) spectra of myricetin NCs in water and raw myricetin in ethanol ($\lambda_{\text{ex}} = 365$ nm). Reproduced with permission from Elsevier.³² Copyright 2022 Elsevier B.V.
(E) Proposed mechanism of the nanocrystal formation by seeding the amorphous NP suspension with existing microcrystals.
(F) XRD patterns of TPE-FN nanoaggregates before and after nanocrystallization.
(G) PL spectra of TPE-FN in crystalline and amorphous states on excitation at 420 nm. The inset shows the photograph of the samples under UV light excitation.
(H) Intravital two-photon fluorescent images of blood vessels of mouse ear skin labeled by TPE-FN nanocrystals and amorphous nanoaggregates. The images at the left panel are collected at 32 μm below the epidermal–dermal junction (excitation at 820 nm and collection with 525/50 filter) and those at the right panel are their 3D images. Reproduced with permission from Wiley.³³ Copyright 2016 WILEY-VCH.

and negligible keto emission were observed in the photoluminescence (PL) spectrum, indicating that the enhanced RIM effect in the crystalline environment remarkably intensified the fluorescence (Figure 3D). Meanwhile, the absorption peak of myricetin NCs was blue-shifted and broadened, which meant the variation of molecular interactions induced by crystallization. Fateminia et al. made a significant breakthrough in the facile synthesis of AIE NCs using ultrasonication.³³ They reported a new AIEgen of TPE-FN, which exhibited moderate emission when forming amorphous orange-emissive NPs in THF/water mixtures. Of interest, natural aging of the as-prepared nanosuspension in the THF/water mixture ($f_w = 70\%$) in the dark for 48 h resulted in the disappearance of yellowish color but the emergence of bright greenish-yellow emission under UV light excitation. SEM images revealed that the morphology of TPE-FN aggregates transformed from spherical NPs, rods to micrometer-long wires. The SAED experiments showed a distinct

spot diffraction pattern for the wires, which confirmed their crystalline features. Apparently, these long wires are inapplicable for bioimaging purposes unless crystal nucleation is maximized and its growth is well controlled within a nanometer scale. Therefore, they proposed a unique strategy of seeding the amorphous nanoaggregates with existing microcrystals of TPE-FN so that the chance of nucleation was increased and molecular packing similar to crystalline seeds was adopted preferably for nucleation. To have the crystal growth confined in the nano range, ultrasonication was utilized to increase the nucleation rate (Figure 3E). Based on the method mentioned above, in the presence of small crystals of TPE-FN, ultrasonication of TPE-FN nanoaggregates for 60 s successfully created the desired NCs, as verified by the X-ray diffraction pattern shown in Figure 3F and the enhanced emission with a 50-nm wavelength blue-shift (Figure 3G). Surprisingly, the obtained crystals still displayed a size of 100 nm, indicative of a perfect nanocrystallization process. To demonstrate the *in vivo* imaging performance, both TPE-FN NCs and amorphous nanoaggregates were applied for the labeling of blood vessels in mouse ear skin. Observation under a two-photon fluorescence microscope at an excitation wavelength of 820 nm showed that NCs were able to visualize both the major blood vessels and smaller capillaries located at 32 μm below the epidermal-dermal junction with higher contrast than the amorphous nanoaggregates (Figure 3H). This was further supported by the brightness difference between their 3D images. It is worth noting that the proposed nanocrystallization method can be generalized to other AIE, room temperature phosphorescence (RTP) and ACQ systems.³⁴ Besides, they utilized the same strategy to enable the nanocrystallization of an AIE photosensitizer to increase its brightness and singlet oxygen generation for phototherapeutic applications, which were mainly contributed by the enhancement in light absorption.³⁵

Nanoconfined crystallization

Controlling the size of crystals is extremely intractable during the nanocrystallization process. Although the ultrasonication method with microcrystals as seeds can modulate both the nucleation and growth rates, the colloidal stability of the prepared NCs is compromised because of the Ostwald ripening that eventually leads to the formation of micron-sized crystals after long-term incubation. When serving as imaging nanoagents in a complex biological environment, bare NCs without any surface functionality might be vulnerable to rapid clearance from the blood after intravenous injection. Therefore, the introduction of biocompatible surfactants to wrap NCs is necessary for biological applications. Meanwhile, considering that the presence of surfactants can hinder the amorphous-to-crystalline transformation process, some technical issues need to be resolved for smooth nanoconfined crystallization. Recently, Prof. Liu's group further developed the strategy of ouzo nanocrystallization of AIEgens in the presence of surfactants.²⁷ First, they performed a systematic analysis on how the crystalline zone varied on the change of AIEgen mass fraction, THF mass fraction or bath sonication time. It was found that the nanocrystal formation was favorable for low AIEgen mass fraction, high THF composition or long sonication time. Second, they explored the ouzo zone for the transformation of amorphous NPs into NCs in the presence of a polymer shell (DSPE-PEG) (Figure 4A). Within the ouzo zone, the co-precipitation of DSPE-PEG and AIEgens in the THF/water mixture could ensure the formation of stable NPs. Beyond the ouzo boundary, DSPE-PEG failed to encapsulate AIEgen aggregates, making their size overlap out of the nanometer range. Through the integration of the crystalline zone and ouzo zone, an idea zone for nanocrystal formation with DSPE-PEG was built successfully (Figure 4A). In a proof-of-concept study, the nanosuspension of an AIEgen named TPA-BDTP was mixed with THF to loosen the core (Figure 4B). By adjusting the THF fraction within the ouzo zone and treatment of sonication, the amorphous NPs of TPA-BDTP were efficiently converted into uniform NCs with a PDI ≈ 0.10 . They also showed that this method was workable for the fabrication of NCs of RTP systems. Freeze-drying is an alternative way to produce drug NCs for improving the dissolution behavior of drugs. The applicability of such an approach is closely associated with the glass transition temperature (T_g) of drugs.^{37,38} Generally, an organic drug with a low T_g is conducive to crystallization. In contrast, for organic AIEgens with a higher T_g , their crystallization via freeze-drying becomes difficult. Facing this challenge, Yan et al. reported a novel methodology to synthesize bright crystalline AIE dots through a sequential nanoprecipitation and freeze-drying process (Figure 4C).³⁶ They established an AIEgen (F1)/acetone/water phase diagram to identify the ouzo domain where the NPs were prepared with optimal colloidal and emissive properties. Subsequently, the nanoprecipitation of F1 was implemented in the presence of different polymeric surfactants as stabilizers, including poly-(vinyl alcohol) (PVA), Pluronic F68, poly(vinylpyrrolidone) (PVP), and poly(vinyl methylether) (PVME), which showed different T_g (Figure 4D). Upon freeze-drying, the obtained powders were redispersed for TEM observation. It was discovered that the use of F68 or PVME endorsed the formation of crystalline AIE dots, whereas the amorphous packing of the NPs was remained with the use of PVA and PVP. As shown in Figure 4D, the mixing of F68 or PVME with F1 ($T_g = 89^\circ\text{C}$)

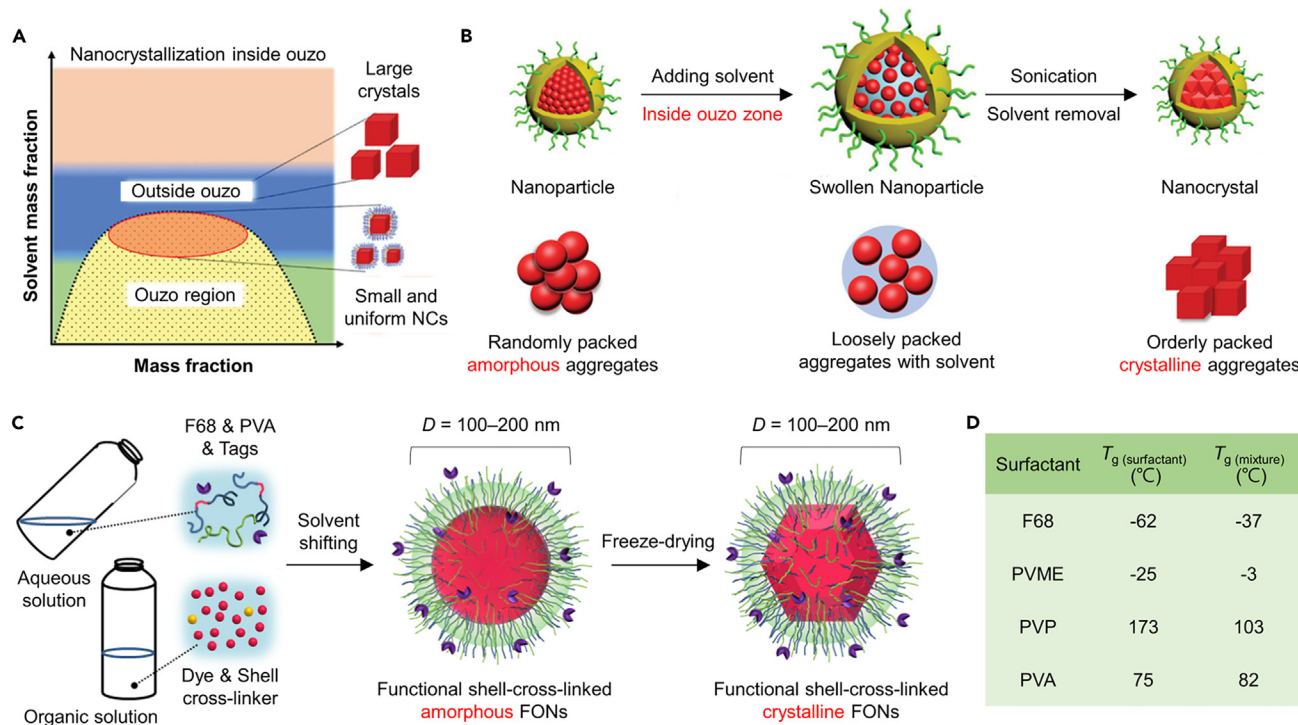


Figure 4. Nanoconfined crystallization

(A) Schematic illustration for systematic encapsulation of nanocrystals by merging the blue-colored crystalline zone of dye with the ouzo zone of polymer. (B) Schematic illustration of formulation of small and uniform organic nanocrystals within the polymer shell (DSPE-PEG) under the ouzo zone of polymer. Reproduced with permission from Wiley.²⁷ Copyright 2021 Wiley-VCH. (C) Schematic illustration of a nanoconfined crystallization strategy to prepare AIE-active crystalline nanoparticles. (D) T_g values of various pure surfactants and surfactant/AIEgen mixtures with 1:1 wt/wt. Reproduced with permission from ACS Publications.³⁶ Copyright 2018 American Chemical Society.

can engender a low T_g value of the binary mixture far below the ambient temperature. Consequently, they reasoned that the plasticization of F1 nanoaggregates provided excellent mobility for the nanocrystallization of F1. To prepare stable water-dispersible NCs of F1 for bioimaging, other than adding F68 as crystallization promoters, PVA and isophorone diisocyanate were also supplemented as surfactants and cross-linkers, respectively (Figure 4C).

MATRIX-ASSISTED RIGIDIFICATION

In addition to strengthen the homotypic interactions between AIEgens through crystallization, the rigidification effect arisen from the encapsulation matrices can be exploited to pose an RIM effect on AIEgens. Hence, the tailoring of heterotypic interactions between matrices and AIEgens is also an important way to improve the brightness of AIE dots. Meanwhile, the biocompatibility of the used matrix is critically essential for biological applications in living systems. In terms of this requirement, endogenous biomacromolecules should be our priority as doping matrices, such as proteins. Besides, synthetically accessible matrices are excellent candidates for preparing water-dispersible AIE dots owing to their vast variety.

Proteins

Natural proteins show numerous inherent advantages than synthetic materials, such as water-solubility, biocompatibility, low toxicity, and biodegradability.³⁹ Serum albumin is the most abundant plasma protein in the blood, and it plays an essential role in transporting various metabolites and nutrients to specific targets.^{40,41} In the past two decades, many advances in human serum albumin (HSA)-based therapeutics have been approved by the Food and Drug Administration (FDA).⁴¹ Meanwhile, HSA is also an ideal matrix for fluorescent imaging materials. For instance, FDA-approved ICG would undergo a severe fluorescence quenching effect in water, whereas the association of ICG with albumin stabilizes the dye and increases its PLQY.⁴² It is conjectured that the strong interaction between fluorophores and albumin would restrict

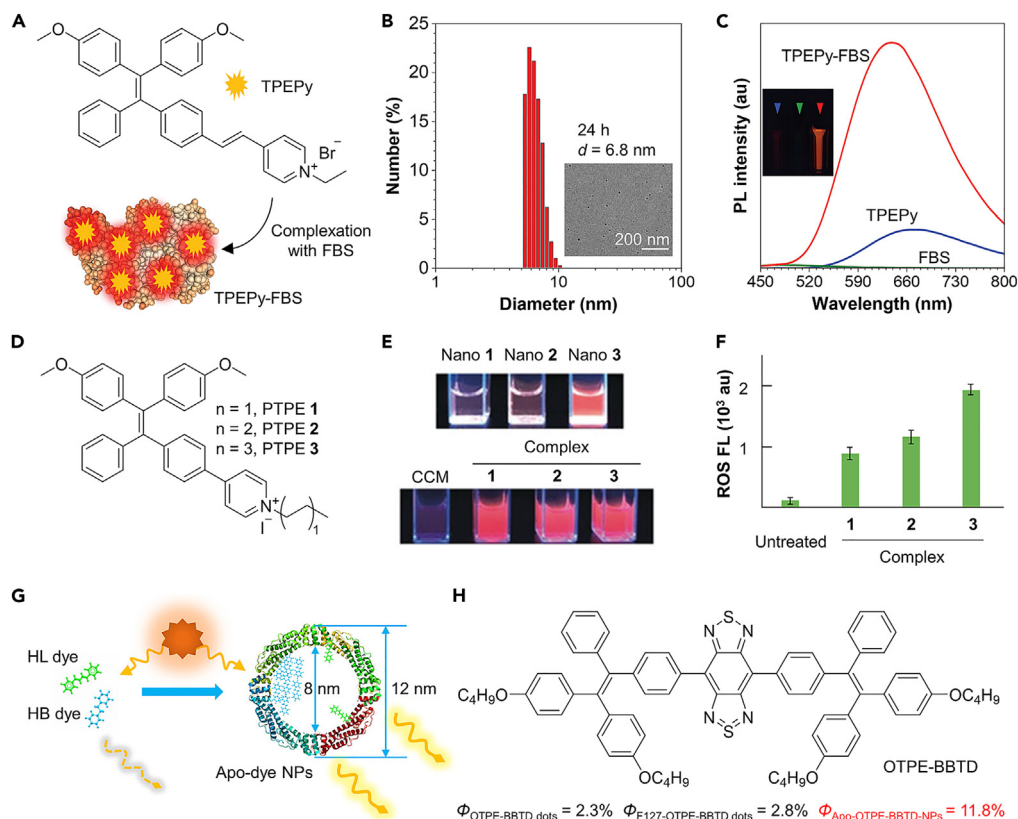


Figure 5. Protein-assisted rigidification

(A) Schematic illustration of TPEPy-FBS nanocomposite preparation.

(B) Hydrodynamic size distribution of TPEPy-FBS in an aqueous medium after 24 h. Inset: TEM image of TPEPy-FBS.

(C) PL spectra of TPEPy, FBS, and TPEPy-FBS in aqueous media. [TPEPy] = 10 μM ; [FBS] = 10% (vol %); $\lambda_{\text{ex}} = 405$ nm. Reproduced with permission from Wiley.⁴⁶ Copyright 2019 WILEY-VCH.

(D) Chemical structures of PTPE 1–3.

(E) Photos of fluorescent solutions of Nano 1–3, complexes 1–3, and CCM taken under UV light.

(F) Comparison of ROS generation in HepG2 cells after treatment with complexes 1–3. Reproduced with permission from Wiley.⁴⁷ Copyright 2020 Wiley-VCH.

(G) Schematic illustration of apo-dye-NPs, where HL and HB dyes are referred to hydrophilic and hydrophobic dyes, respectively.

(H) Chemical structure of OTPE-BBTD and its quantum yields in different states in the aqueous solution. Reproduced with permission from ACS Publications.⁴⁸ Copyright 2021 American Chemical Society.

the molecular motion and block the nonradiative decay pathways of ICG. Because AIEgens emit enhanced fluorescence on structural rigidification, serum albumin with a potential RIM effect could provide an ideal environment for their encapsulation. Qin et al. reported the preparation of bright far-red (FR)/NIR AIE dots using bovine serum albumin (BSA) as a polymer matrix.⁴³ The prepared AIE dots demonstrated superior photostability and high PLQY ($\approx 12\%$) for targeted tumor imaging *in vivo*. Such promising results inspired researchers to explore further using serum albumin.^{44,45} Wang et al. developed a protein-sized AIEgen-protein hybrid nanocomposite (TPEPy-FBS) with bright FR/NIR emission (Figure 5A).⁴⁶ The dynamic light scattering (DLS) analysis and the TEM image showed that TPEPy-FBS was spherical in morphology with an average diameter of less than 10 nm, which was similar to that of FBS. In addition, TPEPy-FBS was very stable in an aqueous solution, as indicated by its steady size distribution after 24 h (Figure 5B). The FBS complexation greatly intensified the fluorescence of TPEPy (Figure 5C). More importantly, TPEPy-FBS exhibited bright two-photon fluorescence and good photostability under femtosecond laser excitation, which was beneficial for *in vivo* imaging with a high signal-to-background ratio (SBR) of about 234. Huang et al. synthesized a series of AIEgens (PTPE 1–3) and explored the influence of different alkyl chains anchored to the pyridinium unit on the photophysical properties when binding to serum albumin (Figure 5D).⁴⁷ PTPE 1–3 could form nanoaggregates (Nano 1–3) in water and showed relatively weak emission.

However, when added to a cell culture medium (CCM), PTPE 1–3 strongly interacted with albumin to form nanocomposites (complex 1–3) with a size of less than 10 nm and emitted much-enhanced fluorescence (Figure 5E). Among these AIEgens, PTPE 3 showed the strongest affinity constant to albumin. The strong interaction with albumin triggered a strong RIM effect on the AIEgens and thus complex 3 showed the strongest ability to generate ROS for phototherapy (Figure 5F). Although albumin is promising in the design of fluorescent contrasting nanoagents, only a few organic dyes have been successfully loaded into albumin or bovine serum. Thus, it is highly desirable to explore other protein carriers. Apoferritin is an existing form of ferritin without combination with iron and its structure can undergo a dissociation-reconstitution process in a pH-sensitive manner.⁴⁹ Thus, Wang et al. reasoned that the hollow nanocavity structure formed by the self-assembly of apoferritin could be used to accommodate a large number of dye molecules, which was promising in the confinement of the aggregates of AIEgens to boost their PLQY (Figure 5G).⁴⁸ OTPE-BBTD was a typical NIR emissive AIEgen, and it could form aggregates in water with a PLQY of 2.3% (Figure 5H). When using a soft F127 to disperse OTPE-BBTD in water, its PLQY slightly increased to 2.8%. However, the PLQY of OTPE-BBTD was boosted to 11.8% after being encapsulated by apoferritin in water, indicating the strong RIM effect generated by the interaction of AIEgens and apoferritin. This strategy was helpful to make full use of the high PLQY of AIEgens for advanced bioimaging.

Rigid polymeric matrices

Polymeric matrices, such as DSPE-PEG and F127, are widely used to disperse hydrophobic fluorophores in an aqueous medium for biomedical applications. However, in most cases, the commonly used polymeric matrix would not provide strong interactions with the intraparticle AIEgens or their aggregates and the resulting weak rigidification significantly compromises their fluorescent brightness. Therefore, the development of highly rigid polymeric matrices can generate a confined microenvironment with a strong RIM effect for the facile preparation of bright AIE dots. Gu et al. utilized corannulene-decorated PEG (Cor-PEG) as a surfactant for the encapsulation of an AIEgen called TPP-TPA to fabricate bright AIE dots (Figure 6A).⁵⁰ The bowl-shaped corannulene possessed superhydrophobicity and hyper-rigidity, which was crucial for the forceful restriction of molecular motion. Compared to the soft DSPE-PEG, the use of Cor-PEG enabled a 4-fold amplified PLQY shown by the resulting AIE dots (Figure 6B). Strikingly, the enhanced RIM effect also increased the ROS production, which ensured a promising effect of cancer phototheranostics. Chen et al. increased the rigidity of the polymeric matrix by introducing calixarene, a type of macrocyclic host to construct supramolecular nanomedicines/imaging agents (Figure 6C).⁵¹ 4-(Dodecyloxy)benzamide-terminated methoxy poly(ethyleneglycol) (PEG-12C) and carboxylic acid modified calix[5]arene pentadecylether (CC5A-12C) were used to prepare water-soluble nanocarriers with high rigidity (S-AIE dots). AIE dots fabricated by using DSPE-PEG served as a comparison. Results showed that the PLQY enhancement in S-AIE dots could reach 31.5 times with a significantly blue-shift in the emission peak (Figure 6D). This result revealed a strong RIM effect and an effectively restricted intramolecular twisting between the electron donor and acceptor, both of which were beneficial for nonradiative decay and emission enhancement. As displayed in Figure 6E, the fluorescence intensity hardly varies even after decreasing the temperature of the solution to 77 K, implying that the intramolecular motion of AIEgens was effectively suppressed by CC5A-12C at room temperature. Fluorescent polystyrene (PS) NPs are commonly used for biomedical sensing and imaging, and their color, decay time, functionalization, and size are widely tunable.⁵³ Meanwhile, they are regarded as highly hydrophobic and rigid polymeric matrices. Thus, encapsulating AIEgens with PS NPs can generate bright AIE dots by taking the advantage of their highly confined intraparticle environment.^{54,55} Bian et al. designed and synthesized ultrabright NPs through the combination of green blue-emissive AIE₄₉₀ and carboxyl-modified PS NPs (Figure 6F).⁵² Owing to the shielding effect of water by the hydrophobic chains of PS and its severe inhibition on the intramolecular motions of AIE₄₉₀, AIE₄₉₀-PS NPs emitted more than 10 times stronger fluorescence than naked AIE₄₉₀ nanoaggregates and were also brighter than AIE₄₉₀-DSPE-PEG NPs (Figure 6G). The prepared PS NPs were further modified with angiotensin-converting enzyme 2 Fc chimera to detect anti-SARS-CoV-2 neutralizing antibodies.

Silicon dioxide

Silica-based NPs are among the first and most widely used in bioimaging.⁵³ They have attracted much attention in biomedical applications in recent decades because of their superior biocompatibility and controllable structures.⁵⁶ Silica nanomaterials play an important role in the development of fluorescent imaging agents. Burns et al. has reported the synthesis of organic dye/silica-based core-shell NPs (Cornell dots), which is currently undergoing a phase II clinical trial for melanoma imaging (NCT02106598).⁵⁷ The experimental data proves that the rigid environment in the silica particle decreases the nonradiative decay rate

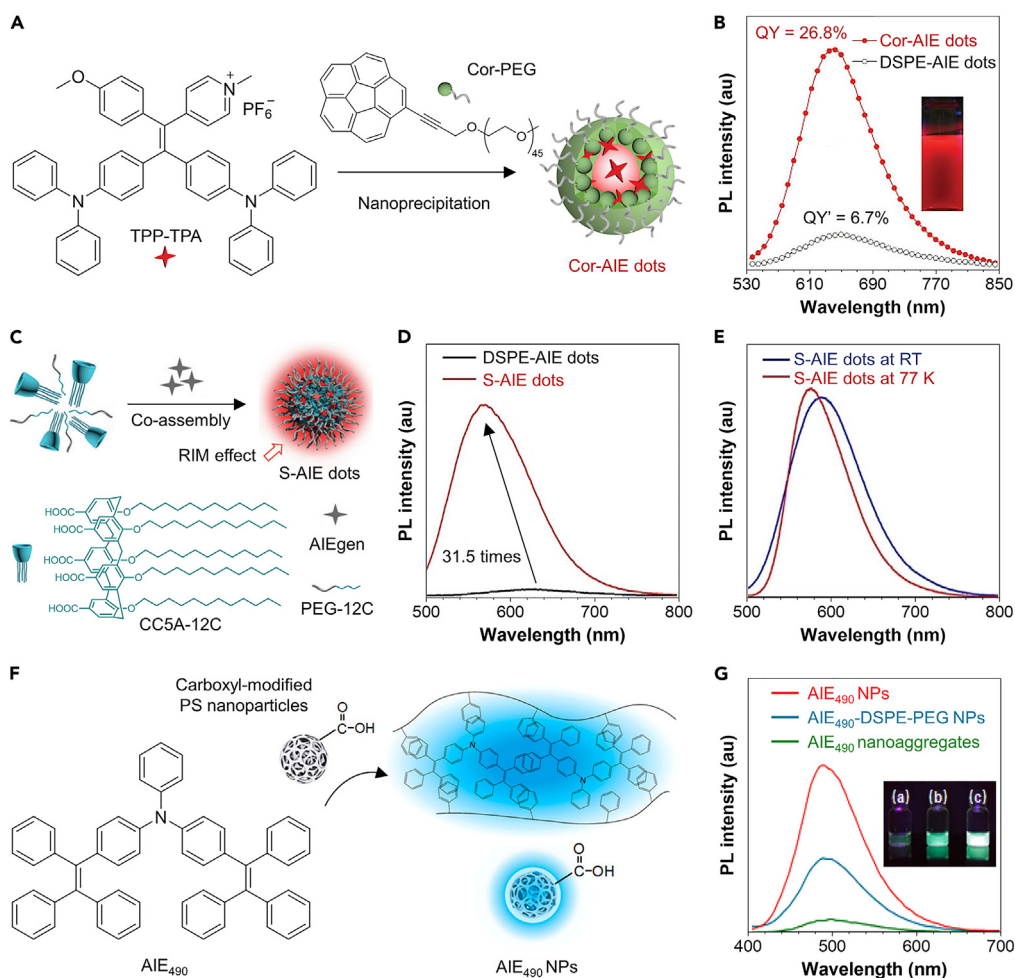


Figure 6. Rigidification by polymeric matrices

(A) Chemical structure of TPP-TPA and schematic illustration for the preparation of Cor-AIE dots.
 (B) PL spectra of Cor-AIE dots and DSPE-AIE dots. $\lambda_{\text{ex}} = 500$ nm. Inset: fluorescent photograph of Cor-AIE dots in solution taken under 365 nm UV lamp. Reproduced with permission from Wiley.⁵⁰ Copyright 2018 WILEY-VCH.
 (C) Schematic illustration for the preparation of S-AIE dots and chemical structure of CC5A-12C.
 (D) PL spectra of S-AIE dots and DSPE-PEG-AIE dots in water. $\lambda_{\text{ex}} = 445$ nm.
 (E) Steady-state PL spectra of S-AIE dots at room temperature and frozen in liquid nitrogen, respectively. Reproduced with permission from Wiley.⁵¹ Copyright 2020 WILEY-VCH.
 (F) Chemical structure of AIE₄₉₀ and schematic illustration of the preparation of AIE₄₉₀ NPs.
 (G) PL spectra of AIE₄₉₀ nanoaggregates, AIE₄₉₀-DSPE-PEG NPs, and AIE₄₉₀ NPs in water. Inset: fluorescent solutions taken under 365 nm UV lamp where inset a is AIE₄₉₀ nanoaggregates, inset b is AIE₄₉₀-DSPE-PEG NPs, and inset c is AIE₄₉₀ NPs. Reproduced with permission from Elsevier.⁵² Copyright 2022 Elsevier Ltd.

and improves the fluorescent brightness. Hence, the introduction of AIEgens into the rigid silica network through physical or chemical methods can produce AIE dots with high fluorescence efficiency and good photostability. Kim et al. prepared silica-based AIE dots through a facile co-precipitation strategy.⁵⁸ The rigidified AIEgen realized two-photon bioimaging with high SBR. Feng et al. demonstrated the importance of the encapsulation approach for an AIEgen namely BTPEAQ by comparing the light emission of AIE dots using the soft matrix (DSPE-PEG) and the rigid matrix (silica shell) (Figure 7A).⁵⁹ The DLS analysis revealed an average hydrodynamic diameter of ~ 7.5 nm for SiO₂-shelled dots, which was suitable for biological applications (Figure 7B). Compared to the AIE dots dispersed by DSPE-PEG, the SiO₂-shelled AIE dots showed a 3-fold higher PL intensity with a PLQY of 12.1% (Figure 7C). As shown in Figure 7D, the SiO₂-shelled dots exhibit an elongated fluorescence lifetime than the polymer-shelled dots, indicating a significant suppression of nonradiative decay pathways of BTPEAQ aggregates inside the silica shell. In addition to the rigidity,

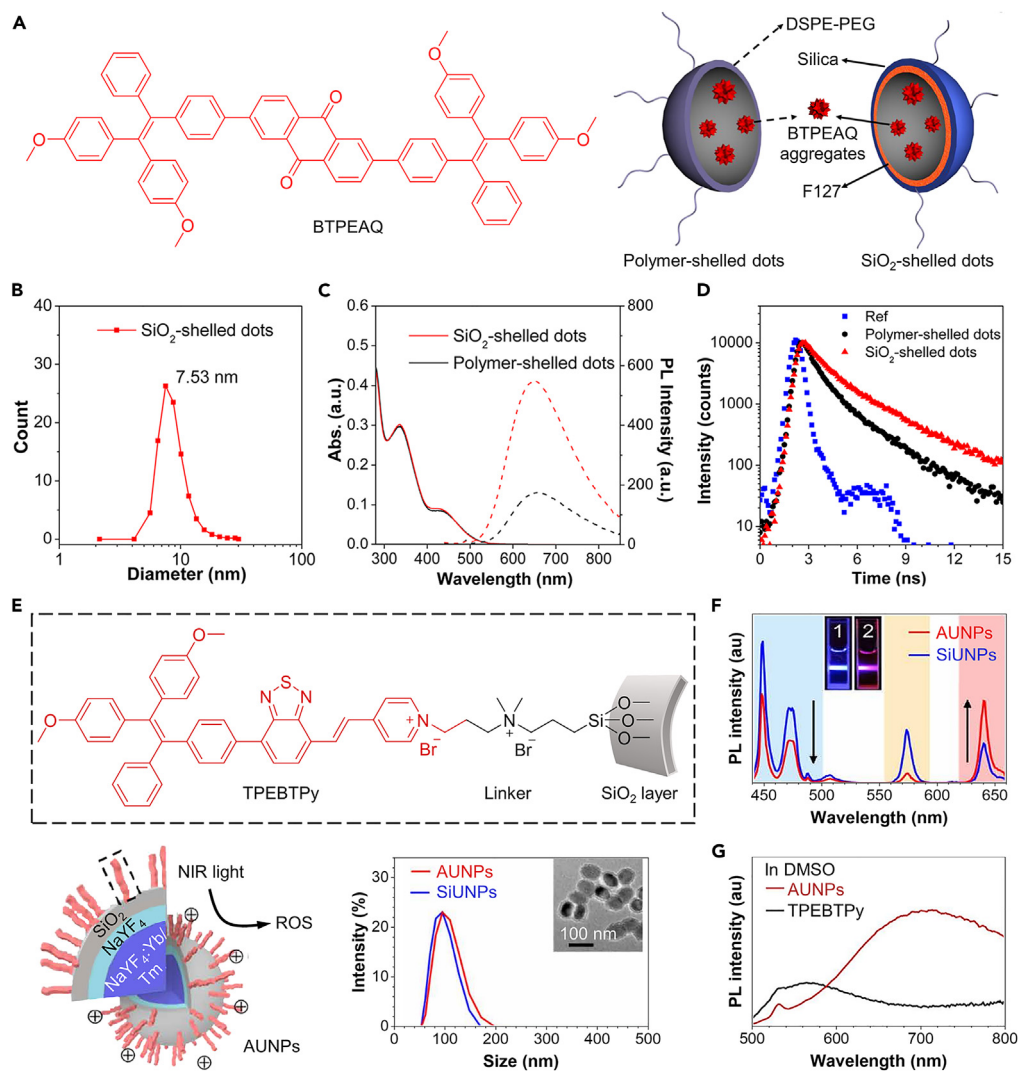


Figure 7. Rigidification by silica-based nanoparticles

(A) Chemical structure of BTPEAQ and schematic illustration of polymer-shelled dots and SiO₂-shelled dots.

(B) Size distribution of SiO₂-shelled dots.

(C) Absorption and PL spectra of different BTPEAQ dots.

(D) Fluorescence decays of BTPEAQ dots at 650 nm in aqueous solution (Black: polymer-shelled dots; red: SiO₂-shelled dots). Instrument response (IRF) (blue) was also indicated. Reproduced with permission from ACS Publications.⁵⁹

Copyright 2016 American Chemical Society.

(E) Structures of TPEBTPy and AUNPs with a dashed box indicating a linked TPEBTPy molecule on the surface of AUNPs and size distributions of AUNPs and SiUNPs. Inset: TEM image of AUNPs.

(F) PL spectra of AUNPs and SiUNPs taken under 980 nm NIR light irradiation. Inset: fluorescent photographs of SiUNPs (1) and AUNPs (2) in PBS taken under 980 nm NIR light irradiation.

(G) PL spectra of AUNPs and TPEBTPy in DMSO. Reproduced with permission from AAAS.⁶⁰ Copyright 2020 The Authors, AAAS.

the functionality of the silica shell enables it as an ideal dye carrier for AIE-based nanomedicine. Thus, the rational design of AIE dots can combine both advantages of silica NPs.^{61,62} Mao et al. coupled an AIE photosensitizer called TPEBTPy with upconversion NPs (UCNPs) via covalent linkage to the silica surface (Figure 7E).⁶⁰ The UCNPs could emit blue light on irradiation of an NIR laser (980 nm), and subsequently the blue light could excite TPEBTPy to generate ROS for anticancer therapy. The DLS analysis and the TEM image revealed that the AIEgen-coupled UCNPs (AUNPs) had a uniform diameter of about 100 nm, which was similar to the precursor SiO₂-UCNPs. On excitation by an NIR laser, the emission of AUNPs markedly

decreased in the blue region, whereas the emission in the red region was enhanced and stronger than that of SiUNPs (Figure 7F). The change of the upconversion PL spectrum indicated an efficient energy-transfer process between TPEBTPy and UCNPs. The enhancement in the red emission implied suppressed nonradiative decay of the AIEgen. Moreover, the PL spectra of TPEBTPy and AUNPs in DMSO were measured. As shown in Figure 7G, the emission of TPEBTPy increased significantly after being linked to the silica surface, indicating the activation of the AIE property because of the RIM effect.

Conclusions and outlook

At the molecular level, the flexible manipulation of building blocks of AIEgens, including donors, acceptors, and π bridges, provides many possibilities for the construction of highly emissive AIE dots. More importantly, the ultimate brightness of AIE dots is also determined by aggregate-state molecular packing based on intermolecular interactions, which are divided into homotypic interactions between AIEgens and heterotypic interactions between matrices and AIEgens. Such an exploration at the aggregate level is of profound value for the deep grasp of how microscopic molecular packing magically influences macroscopic photoluminescent properties of bulk counterparts and further guides the molecular design toward a desired molecular packing and fluorescent outcome.

As an efficient approach to promote the homotypic interactions between AIEgens, nanocrystallization can restrict the molecular motion of AIEgens to a higher degree for improving the brightness and photostability of AIE dots. Several strategies have been elaborated in this review, such as natural aging, sonication-augmented crystallization, nanoconfined crystallization, etc. However, there is still no perfect method that can address all the existing technical issues. For example, nanocrystallization augmented by sonication is a widely applicable process for the facile synthesis of NCs of AIEgens, but the availability of seeds is a prerequisite. Moreover, the scalability of this process is skeptical. Freeze-drying of amorphous NPs in the presence of plasticizing agents has been proven to be a scalable way to produce NCs, although it normally takes a long time for the complete sublimation of the used solvent. Therefore, there is much room for the optimization of the nanocrystallization process. In addition, nanocrystallization can also be applied to the preparation of pure organic NCs with persistent luminescence, which is envisioned to greatly increase the SBR in bioimaging.^{63–65}

Given that the dispersibility of AIE dots in the biological environment leans on the use of matrices, enhancing the heterotypic interactions between the selected matrices and AIEgens is an optional way to improve their emission efficiency. As previously illustrated, the currently used matrices are composed of proteins, rigid polymeric matrices, and silicon dioxide. Obviously, these matrices are superior to soft matrices, such as DSPE-PEG and F127, in terms of their strong interactions with AIEgens. However, until now, both DSPE-PEG and F127 are still among the most widely used polymeric matrices when fabricating AIE dots because of their commercial availability and ease of use. Although the use of rigid matrices can enhance the emission of AIEgens, the fabrication method of AIE dots using these matrices lacks wide applicability or requires synthetic skills and experience. For example, proteins only assemble with a limited portion of AIEgens with functional groups to form nanocomplexes. The synthesis of polymeric matrices and silicon dioxide is somehow convoluted so researchers usually prefer to purchase DSPE-PEG and F127 for the preparation of AIE dots. Therefore, future endeavors should be given to the development of rigid matrices with characteristics such as ease of synthesis and wide applicability. Besides, in view of the vital importance of biocompatibility of the used matrices, we hope that exceptional efforts will be devoted to the development of biogenic rigid matrices.

ACKNOWLEDGMENTS

This work was financially supported by the National Natural Science Foundation of China (21788102), the Research Grants Council of Hong Kong (16306620, 16303221, N_HKUST609/19, and C6014-20W), the Innovation and Technology Commission (ITC-CNERC14SC01 and ITCPCD/17-9), and the Natural Science Foundation of Guangdong Province (2019B121205002).

AUTHOR CONTRIBUTIONS

C.X., H.S., and J.W.Y.L. conceived the review. C.X. and H.S. researched and analyzed the data. C.X. and H.S. wrote the manuscript. J.W.Y.L., R.T.T.K., and T.-M.L. revised and proofread the manuscript. J.W.Y.L. and B.Z.T. acquired funding. All authors have given approval to the final version of the manuscript.

DECLARATION OF INTERESTS

The authors declare no competing interests.

REFERENCES

1. Brewster, D. (1846). XIII.—on the decomposition and dispersion of light within solid and fluid bodies. *Trans. R. Soc. Edinb. Earth Sci.* 16, 111–121.
2. Xu, C., Ye, R., Shen, H., Lam, J.W.Y., Zhao, Z., and Zhong Tang, B. (2022). Molecular motion and nonradiative decay: towards efficient photothermal and photoacoustic systems. *Angew. Chem. Int. Ed. Engl.* 61, e202204604.
3. Herschel, J.F.W. (1845). IV. Ἀμόρφωτα, no. I.—on a case of superficial colour presented by a homogeneous liquid internally colourless. *Philos. Trans. R. Soc. Lond.* 143–145.
4. Stokes, G.G. (1852). XXX. On the change of refrangibility of light. *Philos. Trans. R. Soc. Lond.* 463–562.
5. Morton, H. (1871). Notes on the color of fluorescent solutions. *J. Franklin Inst.* 92, 426–428.
6. Hagenbach, E. (1873). VI. Experiments on fluorescence. *Lond. Edinb. Dublin Philos. Mag. J. Sci.* 45, 57–64.
7. Zhang, H., Zhao, Z., Turley, A.T., Wang, L., McGonigal, P.R., Tu, Y., Li, Y., Wang, Z., Kwok, R.T.K., Lam, J.W.Y., and Tang, B.Z. (2020). Aggregate science: from structures to properties. *Adv. Mater.* 32, 2001457.
8. Morton, H. (1871). Observations on the colour of fluorescent solutions. *Lond. Edinb. Dublin Philos. Mag. J. Sci.* 42, 393–395.
9. Zink, J.I. (1975). Triboluminescence of uranyl nitrate. *Inorg. Chem.* 14, 555–558.
10. Tuijtel, M.W., Mulder, A.A., Posthuma, C.C., van der Hoeven, B., Koster, A.J., Bárcena, M., Faas, F.G.A., and Sharp, T.H. (2017). Inducing fluorescence of uranyl acetate as a dual-purpose contrast agent for correlative light-electron microscopy with nanometre precision. *Sci. Rep.* 7, 10442.
11. Würthner, F., Sens, R., Etzbach, K.H., and Seybold, G. (1999). Design, synthesis, and evaluation of a dye library: glass-forming and solid-state luminescent merocyanines for functional materials. *Angew. Chem. Int. Ed. Engl.* 38, 1649–1652.
12. Deans, R., Kim, J., Machacek, M.R., and Swager, T.M. (2000). A poly(p-phenyleneethynylene) with a highly emissive aggregated phase. *J. Am. Chem. Soc.* 122, 8565–8566.
13. Luo, J., Xie, Z., Lam, J.W.Y., Cheng, L., Tang, B.Z., Chen, H., Qiu, C., Kwok, H.S., Zhan, X., Liu, Y., and Zhu, D. (2001). Aggregation-induced emission of 1-methyl-1, 2, 3, 4, 5-pentaphenylsilole. *Chem. Commun.* 1740–1741.
14. Zhao, Z., Zhang, H., Lam, J.W.Y., and Tang, B.Z. (2020). Aggregation-induced emission: new vistas at the aggregate level. *Angew. Chem. Int. Ed. Engl.* 59, 9888–9907.
15. Dong, Y., Lam, J.W.Y., Qin, A., Liu, J., Li, Z., Tang, B.Z., Sun, J., and Kwok, H.S. (2007). Aggregation-induced emissions of tetraphenylethene derivatives and their utilities as chemical vapor sensors and in organic light-emitting diodes. *Appl. Phys. Lett.* 91, 011111.
16. Shi, J., Chang, N., Li, C., Mei, J., Deng, C., Luo, X., Liu, Z., Bo, Z., Dong, Y.Q., and Tang, B.Z. (2012). Locking the phenyl rings of tetraphenylethene step by step: understanding the mechanism of aggregation-induced emission. *Chem. Commun.* 48, 10675–10677.
17. Ding, D., Li, K., Liu, B., and Tang, B.Z. (2013). Bioprobes based on AIE fluorogens. *Acc. Chem. Res.* 46, 2441–2453.
18. Feng, G., and Liu, B. (2018). Aggregation-induced emission (AIE) dots: emerging theranostic nanolights. *Acc. Chem. Res.* 51, 1404–1414.
19. Xu, C., Peng, C., Yang, X., Zhang, R., Zhao, Z., Yan, B., Zhang, J., Gong, J., He, X., Kwok, R.T.K., et al. (2022). One-pot synthesis of customized metal-phenolic-network-coated AIE dots for in vivo bioimaging. *Adv. Sci.* 9, 2104997.
20. Zhang, J., Li, A., Zou, H., Peng, J., Guo, J., Wu, W., Zhang, H., Zhang, J., Gu, X., Xu, W., et al. (2020). A “simple” donor-acceptor AIEgen with multi-stimuli responsive behavior. *Mater. Horiz.* 7, 135–142.
21. Tong, S., Dai, J., Sun, J., Liu, Y., Ma, X., Liu, Z., Ma, T., Tan, J., Yao, Z., Wang, S., et al. (2022). Fluorescence-based monitoring of the pressure-induced aggregation microenvironment evolution for an AIEgen under multiple excitation channels. *Nat. Commun.* 13, 5234.
22. Qian, H., Cousins, M.E., Horak, E.H., Wakefield, A., Liptak, M.D., and Aprahamian, I. (2017). Suppression of Kasha’s rule as a mechanism for fluorescent molecular rotors and aggregation-induced emission. *Nat. Chem.* 9, 83–87.
23. Chen, S., Öhman, C., Jefferies, S.R., Gray, H., Xia, W., and Engqvist, H. (2016). Fabrication of fluorescent nanoparticles based on AIE luminogens (AIE dots) and their applications in bioimaging. *Mater. Horiz.* 6, 283–289.
24. Dong, Y., Lam, J.W.Y., Qin, A., Li, Z., Sun, J., Sung, H.H.-Y., Williams, I.D., and Tang, B.Z. (2007). Switching the light emission of (4-biphenyl) phenylidibenzofulvene by morphological modulation: crystallization-induced emission enhancement. *Chem. Commun.* 40–42.
25. He, X., Xie, H., Hu, L., Liu, P., Xu, C., He, W., Du, W., Zhang, S., Xing, H., Liu, X., et al. (2021). A versatile AIE fluorogen with selective reactivity to primary amines for monitoring amination, protein labeling, and mitochondrial staining. *Aggregate*, e239.
26. Shen, H., Sun, F., Zhu, X., Zhang, J., Ou, X., Zhang, J., Xu, C., Sung, H.H.Y., Williams, I.D., Chen, S., et al. (2022). Rational design of NIR-II AIEgens with ultrahigh quantum yields for photo- and chemiluminescence imaging. *J. Am. Chem. Soc.* 144, 15391–15402.
27. Middha, E., Chen, C., Manghnani, P.N., Wang, S., Zhen, S., Zhao, Z., and Liu, B. (2022). Synthesis of uniform polymer encapsulated organic nanocrystals through ozo nanocrystallization. *Small Methods* 6, 2100808.
28. Zheng, Z., Li, D., Liu, Z., Peng, H.Q., Sung, H.H.Y., Kwok, R.T.K., Williams, I.D., Lam, J.W.Y., Qian, J., and Tang, B.Z. (2019). Aggregation-induced nonlinear optical effects of AIEgen nanocrystals for ultradeep in vivo bioimaging. *Adv. Mater.* 31, 1904799.
29. Xu, R., Dang, D., Wang, Z., Zhou, Y., Xu, Y., Zhao, Y., Wang, X., Yang, Z., and Meng, L. (2022). Facilely prepared aggregation-induced emission (AIE) nanocrystals with deep-red emission for super-resolution imaging. *Chem. Sci.* 13, 1270–1280.
30. Xu, R., Chi, W., Zhao, Y., Tang, Y., Jing, X., Wang, Z., Zhou, Y., Shen, Q., Zhang, J., Yang, Z., et al. (2022). All-in-one theranostic platforms: deep-red AIE nanocrystals to target dual-organelles for efficient photodynamic therapy. *ACS Nano* 16, 20151–20162.
31. Koenig, M., Torres, T., Barone, V., Brancato, G., Guldi, D.M., and Bottari, G. (2014). Ultrasound-induced transformation of fluorescent organic nanoparticles from a molecular rotor into rhomboidal nanocrystals with enhanced emission. *Chem. Commun.* 50, 12955–12958.
32. Li, F., Zhe, T., Ma, K., Zhang, Y., Li, R., Cao, Y., Li, M., and Wang, L. (2023). One stone two birds: multifunctional flavonol nanocrystals enable food packaging to both preserve freshness and visually monitor freshness. *Chem. Eng. J.* 453, 139760.
33. Fatemina, S.M.A., Wang, Z., Goh, C.C., Manghnani, P.N., Wu, W., Mao, D., Ng, L.G., Zhao, Z., Tang, B.Z., and Liu, B. (2017). Nanocrystallization: a unique approach to yield bright organic nanocrystals for biological applications. *Adv. Mater.* 29, 1604100.
34. Nicol, A., Kwok, R.T.K., Chen, C., Zhao, W., Chen, M., Qu, J., and Tang, B.Z. (2017). Ultrafast delivery of aggregation-induced emission nanoparticles and pure organic phosphorescent nanocrystals by saponin encapsulation. *J. Am. Chem. Soc.* 139, 14792–14799.

35. Fatemina, S.M.A., Kacenauskaite, L., Zhang, C.J., Ma, S., Manghnani, P.N., Manghnani, P.N., Chen, J., Xu, S., Hu, F., Xu, B., et al. (2018). Simultaneous increase in brightness and singlet oxygen generation of an organic photosensitizer by nanocrystallization. *Small* 14, 1803325.
36. Yan, X., Remond, M., Zheng, Z., Hoibian, E., Soulage, C., Chambert, S., Andraud, C., Van der Sanden, B., Ganachaud, F., Bretonnière, Y., and Bernard, J. (2018). General and scalable approach to bright, stable, and functional AIE fluorogen colloidal nanocrystals for in vivo imaging. *ACS Appl. Mater. Interfaces* 10, 25154–25165.
37. De Waard, H., Hinrichs, W.L.J., and Frijlink, H.W. (2008). A novel bottom-up process to produce drug nanocrystals: controlled crystallization during freeze-drying. *J. Control. Release* 128, 179–183.
38. Fatemina, S.M.A., Wang, Z., and Liu, B. (2017). Nanocrystallization: an effective approach to enhance the performance of organic molecules. *Small Methods* 1, 1600023.
39. Liu, X., Wang, C., and Liu, Z. (2018). Protein-engineered biomaterials for cancer theranostics. *Adv. Healthc. Mater.* 7, 1800913.
40. Liu, Z., and Chen, X. (2016). Simple bioconjugate chemistry serves great clinical advances: albumin as a versatile platform for diagnosis and precision therapy. *Chem. Soc. Rev.* 45, 1432–1456.
41. Rahimizadeh, P., Yang, S., and Lim, S.I. (2020). Albumin: an emerging opportunity in drug delivery. *Biotechnol. Bioprocess Eng.* 25, 985–995.
42. Carr, J.A., Franke, D., Caram, J.R., Perkinson, C.F., Saif, M., Askoxylakis, V., Datta, M., Fukumura, D., Jain, R.K., Bawendi, M.G., and Bruns, O.T. (2018). Shortwave infrared fluorescence imaging with the clinically approved near-infrared dye indocyanine green. *Proc. Natl. Acad. Sci. USA* 115, 4465–4470.
43. Qin, W., Ding, D., Liu, J., Yuan, W.Z., Hu, Y., Liu, B., and Tang, B.Z. (2012). Biocompatible nanoparticles with aggregation-induced emission characteristics as far-red/near-infrared fluorescent bioprobes for in vitro and in vivo imaging applications. *Adv. Funct. Mater.* 22, 771–779.
44. Gao, S., Wei, G., Zhang, S., Zheng, B., Xu, J., Chen, G., Li, M., Song, S., Fu, W., Xiao, Z., and Lu, W. (2019). Albumin tailoring fluorescence and photothermal conversion effect of near-infrared-II fluorophore with aggregation-induced emission characteristics. *Nat. Commun.* 10, 2206.
45. Liu, Z., Zhang, J., Liu, H., Shen, H., Meng, N., Qi, X., Ding, K., Song, J., Fu, R., Ding, D., and Feng, G. (2023). BSA-AIE nanoparticles with boosted ROS generation for immunogenic cell death immunotherapy of multiple myeloma. *Adv. Mater.* 35, 2208692.
46. Wang, S., Hu, F., Pan, Y., Ng, L.G., and Liu, B. (2019). Bright AIEgen-protein hybrid nanocomposite for deep and high-resolution in vivo two-photon brain imaging. *Adv. Funct. Mater.* 29, 1902717.
47. Huang, Y., You, X., Wang, L., Zhang, G., Gui, S., Jin, Y., Zhao, R., and Zhang, D. (2020). Pyridinium-substituted tetraphenylethylenes functionalized with alkyl chains as autophagy modulators for cancer therapy. *Angew. Chem. Int. Ed. Engl.* 59, 10042–10051.
48. Wang, X., Wang, X., Qu, B., Alifu, N., Qi, J., Liu, R., Fu, Q., Shen, R., Xia, Q., Wu, L., et al. (2022). A class of biocompatible dye-protein complex optical nanoprobes. *ACS Nano* 16, 328–339.
49. Wang, X., Chen, L., Su, X., and Ai, S. (2013). Electrochemical immunosensor with graphene quantum dots and apoferritin-encapsulated Cu nanoparticles double-assisted signal amplification for detection of avian leukosis virus subgroup. *Biosens. Bioelectron.* 47, 171–177.
50. Gu, X., Zhang, X., Ma, H., Jia, S., Zhang, P., Zhao, Y., Liu, Q., Wang, J., Zheng, X., Lam, J.W.Y., et al. (2018). Corannulene-incorporated AIE nanodots with highly suppressed nonradiative decay for boosted cancer phototheranostics in vivo. *Adv. Mater.* 30, 1801065.
51. Chen, C., Ni, X., Tian, H.-W., Liu, Q., Guo, D.-S., and Ding, D. (2020). Calixarene-based supramolecular AIE dots with highly inhibited nonradiative decay and intersystem crossing for ultrasensitive fluorescence image-guided cancer surgery. *Angew. Chem. Int. Ed. Engl.* 59, 10008–10012.
52. Bian, L., Li, Z., He, A., Wu, B., Yang, H., Wu, Y., Hu, F., Lin, G., and Zhang, D. (2022). Ultrabright nanoparticle-labeled lateral flow immunoassay for detection of anti-SARS-CoV-2 neutralizing antibodies in human serum. *Biomaterials* 288, 121694.
53. Wolfbeis, O.S. (2015). An overview of nanoparticles commonly used in fluorescent bioimaging. *Chem. Soc. Rev.* 44, 4743–4768.
54. Yuan, H., Li, Z., Bai, H., Chen, Z., Yao, C., Jia, S., Li, L., Qi, R., and Zhao, C.-H. (2021). Aggregation-induced emission nanoparticles with NIR and photosensitizing characteristics for resistant bacteria elimination and real-time tracking. *Mater. Chem. Front.* 5, 6611–6617.
55. Chen, R., Ren, C., Liu, M., Ge, X., Qu, M., Zhou, X., Liang, M., Liu, Y., and Li, F. (2021). Early detection of SARS-CoV-2 seroconversion in humans with aggregation-induced near-infrared emission nanoparticle-labeled lateral flow immunoassay. *ACS Nano* 15, 8996–9004.
56. Yang, Y., Zhang, M., Song, H., and Yu, C. (2020). Silica-based nanoparticles for biomedical applications: from nanocarriers to biomodulators. *Acc. Chem. Res.* 53, 1545–1556.
57. Burns, A., Ow, H., and Wiesner, U. (2006). Fluorescent core-shell silica nanoparticles: towards "Lab on a Particle" architectures for nanobiotechnology. *Chem. Soc. Rev.* 35, 1028–1042.
58. Kim, S., Pudavar, H., Bonoiu, A., and Prasad, P. (2007). Aggregation-enhanced fluorescence in organically modified silica nanoparticles: a novel approach toward high-signal-output nanoprobes for two-photon fluorescence bioimaging. *Adv. Mater.* 19, 3791–3795.
59. Feng, G., Wu, W., Xu, S., and Liu, B. (2016). Far red/near-infrared AIE dots for image-guided photodynamic cancer cell ablation. *ACS Appl. Mater. Interfaces* 8, 21193–21200.
60. Mao, D., Hu, F., Yi, Z., Kenry, X., Yan, S., Luo, Z., Wu, W., Wang, Z., Kong, D., et al. (2020). AIEgen-coupled upconversion nanoparticles eradicate solid tumors through dual-mode ROS activation. *Sci. Adv.* 6, eabb2712.
61. Li, Q.-L., Wang, D., Cui, Y., Fan, Z., Ren, L., Li, D., and Yu, J. (2018). AIEgen-functionalized mesoporous silica gated by cyclodextrin-modified CuS for cell imaging and chemophotothermal cancer therapy. *ACS Appl. Mater. Interfaces* 10, 12155–12163.
62. Li, J., Leung, C.W.T., Wong, D.S.H., Xu, J., Li, R., Zhao, Y., Yung, C.Y.Y., Zhao, E., Tang, B.Z., and Bian, L. (2019). Photocontrolled siRNA delivery and biomarker-triggered luminogens of aggregation-induced emission by up-conversion NaYF₄:Yb³⁺Tm³⁺@SiO₂ nanoparticles for inducing and monitoring stem-cell differentiation. *ACS Appl. Mater. Interfaces* 11, 22074–22084.
63. Zhang, X., Du, L., Zhao, W., Zhao, Z., Xiong, Y., He, X., Gao, P.F., Alam, P., Wang, C., Li, Z., et al. (2019). Ultralong UV/mechano-excited room temperature phosphorescence from purely organic cluster excitons. *Nat. Commun.* 10, 5161.
64. Alam, P., Leung, N.L.C., Liu, J., Cheung, T.S., Zhang, X., He, Z., Kwok, R.T.K., Lam, J.W.Y., Sung, H.H.Y., Williams, I.D., et al. (2020). Two are better than one: a design principle for ultralong-persistent luminescence of pure organics. *Adv. Mater.* 32, 2001026.
65. Alam, P., Cheung, T.S., Leung, N.L.C., Zhang, J., Guo, J., Du, L., Kwok, R.T.K., Lam, J.W.Y., Zeng, Z., Phillips, D.L., et al. (2022). Organic long-persistent luminescence from a single-component aggregate. *J. Am. Chem. Soc.* 144, 3050–3062.